51st AIAA Aerospace Sciences Meeting including the New Horizons Forum and Aerospace Exposition
07 - 10 January 2013, Grapevine (Dallas/Ft. Worth Region), Texas

AIAA 2013-0857

Check for updates

A High-Order Self-Adaptive Monolithic Solver for Viscous-Inviscid Interacting Flows

D. Moro*, N. C. Nguyen†, M. Drela‡ and J. Peraire§
Massachusetts Institute of Technology, Cambridge, MA 02139, USA

We present a high-order self-adaptive monolithic method for solving viscous-inviscid interaction problems. The defect formulation is used to segregate the viscous and inviscid effects and couple them at the wall using the integrated defects for the conserved quantities, thereby allowing the overlap of the inviscid and boundary layer meshes. In particular, the viscous mesh will be extruded from the surface of the body or the wake in a given direction (obtained from a preprocess step) according to a normal scaling scalar variable δ. This normal scaling quantity satisfies a partial differential equation on the surface of the body or wake and will be evolved as part of the solution process. This allows the viscous mesh to be adapted to the thickness of the boundary layer in an automated manner. The viscous and inviscid parts of the system are discritized using a high order Hybridizable Discontinuous Galerkin (HDG) scheme while the normal scaling equation is discretized using a Surface Finite Element Method (SFEM). The system is solved in a monolithic manner. We present results in 2D for simple laminar and turbulent flows to validate the solver.

Downloaded by MIT LIBRARIES on August 16, 2022 | http://arc.aiaa.org | DOI: 10.2514/6.2013-857

I. Motivation

In the last decade, the advances in high order schemes have significantly pushed the state of the art in solvers for aerodynamic applications. These high order schemes come in several variants: Discontinuous Galerkin (DG), Spectral Finite Differences (SD) and Spectral Finite Volumes (SV) each with its associated advantages and disadvantages. Of particular success for complex geometries are the schemes that are based on the RANS equations on unstructured grids such as DG,[1–3] especially when they are combined with an adaptivity procedure to take advantage of the asymptotic convergence rate of the high order approximation.[4,5] Despite these very promising results, DG schemes are far from being widely used in the industry for several reasons.

First, they are considered computationally expensive unless very high levels of accuracy are required, in which case the higher order of convergence quickly leverages the cost.[6]

Also, high order mesh generation is not mature enough to reliably produce good quality anisotropic meshes for complex geometries in an automated fashion. Several researchers have looked at the problem with more or less success using PDE based techniques to deform the mesh and conform to the boundaries of the domain[7] while others use cut-cells to generate the high order mesh from an initial non-conforming anisotropic mesh.[6] In any case there is no clear solution to the problem yet.

Finally, high order schemes are generally believed to present robustness issues in certain situations such as shock waves or under-resolved boundary layers. In general, it is widely agreed that this is related to the oscillations that high order approximations may suffer when the solution is not regular enough or there is not enough resolution (for a given combination of approximation order and mesh size), that may move the solution into non-physical values and produce a sudden divergence of the computations. Several researchers have proposed different ways to alleviate this issues, that range from the use of artificial viscosity[8,9] to modified numerical schemes[10] or regularized fluid models.[11]

*PhD Candidate, AIAA Student Member.
†Research Scientist, AIAA Member.
‡Terry J. Kohler Professor of Fluid Dynamics, AIAA Fellow.
§H. N. Slater Professor of Aeronautics and Astronautics, AIAA Fellow.

Copyright © 2013 by the American Institute of Aeronautics and Astronautics, Inc. All rights reserved.

All this issues together make high order schemes impossible to implant on a design environment, where the engineer might have to run dozens of configurations and iterate the design along the way, and does not have time to spend on fixing meshes and close watching convergence. In this situation, faster and more robust tools are preferred over high order methods (or low order Navier-Stokes solvers) even if they simplify the physics of the problem. The best example of this kind of tool would be the TRANAIR code[12] that sees heavy use across The Boeing Company.[13,14] The success of TRANAIR is due to several reasons: first, it does not require the user to generate an initial mesh and only the geometry of the body has to be defined, second, it performs adaptation in an automated manner, third, it solves the full-potential equations and hence can model compressibility effects, and last, it uses a far-field correction to truncate the domain of the solution and reduce the computation to a fraction of what it would take any Navier-Stokes solver for the same problem.

To account for viscous effects, TRANAIR is combined with a fully-coupled 2D streamline integral boundary layer method. The results obtained agree well with experiments for a wide range of cases, provided 3D effects in the boundary layer are not important. This limits the accuracy of the predictions in regions like the wing-body junction or engines nacelles or in cases where flow might separate. Furthermore, the advent of new aircraft concepts like the ones derived from NASA's N+3 project, will bring a change of paradigm in which the different elements of the aircraft (wing, fuselage, engines, etc.) will be more closely integrated and hence less prone to independent analysis or simplified interaction assumptions. In this situation, designers will require a tool that models 3D viscous effects and provides solutions in a reasonable time in a robust way.

It seems reasonable to think that a segregation of the viscous effects from the inviscid flow using interactive boundary layer theory (IBLT), as done in TRANAIR, would help achieve this goal. The next critical step would be to deal with the boundary layer in an efficient way. Following the success of 2D coupled integral boundary layer formulations,[15–17] several 3D integral boundary layer models have been proposed using 3 or 4 equations and closure coefficients to parametrize the 3D profiles.[18,19] These models have not seen widespread use due to several reasons, the most important being how hard they are to calibrate for general flows compared to their 2D counterparts.

Another approach would consist of a differential method where the RANS equations are solved wherever viscous effects are important.[20] A significant advantage of this approach is the independence of the solution with respect to closure functions and calibration (other than the turbulence model used). However, this approach requires an efficient way of computing the viscous flows and the generation of a mesh that does not extend into the inviscid flow. If any of these two requirements is not satisfied the whole purpose of the IBLT segregation would be defeated.

In this work we propose to use the IBLT approach solving the Euler equations in the whole domain together with the Defect formulation of the Navier-Stokes equations[21,22] on a mesh extruded from the surface mesh and overlapping with the inviscid domain. The coupling between both domains will happen at the wall using the integrated defects across the boundary layer. To obtain the best accuracy for a given computational effort, the discretization of the equations will be carried out using a high order Discontinuous Galerkin method, and the extruded mesh thickness will be computed as part of the solution to follow the boundary layer profile.[20] This way, we combine the advantages of an adapted grid with a high order approximation at the cost of an extra equation on the surface to account for the thickness. In order to accommodate the grid evolution, an Arbitrary Lagrangean-Eulerian (ALE) formulation of the defect equations will be used. Using the ALE formulation, the equations are solved on a reference domain, that in this case is the tensor product of a surface grid and a 1D normal grid, and is never formed explicitly.

In what follows, we will first present the formulation of the problem, followed by the discretization schemes used. Continuing, some preliminary results using this approach will be presented for flat plate flows. Conclusions and expected contributions will be discussed last.

II. Formulation

The problem of compressible viscous flow can described by the Favre-Averaged Navier-Stokes equations that written in conservation form read:

$$\frac{\partial \mathbf{u}}{\partial t} + \nabla \cdot \mathbf{F} = \nabla \cdot \mathbf{G}, \tag{1}$$

Downloaded by MIT LIBRARIES on August 16, 2022 | http://arc.aiaa.org | DOI: 10.2514/6.2013-857

where:

$$\mathbf{u} = \begin{bmatrix} \rho \\ \rho v_1 \\ \rho v_2 \\ \rho v_3 \\ \rho E \end{bmatrix}, \qquad \mathbf{F}_i = \begin{bmatrix} \rho v_i \\ \rho v_i v_1 + p\delta_{i1} \\ \rho v_i v_2 + p\delta_{i2} \\ \rho v_i v_3 + p\delta_{i3} \\ \rho v_i H \end{bmatrix}, \qquad \mathbf{G}_i = \begin{bmatrix} 0 \\ \tau_{1i} \\ \tau_{2i} \\ \tau_{3i} \\ \sum_{j=1}^{d} \tau_{ij} u_j + q_i \end{bmatrix}, \tag{2}$$

$$\tau_{ij} = \bar{\mu}\left(\frac{\partial v_i}{\partial x_j} + \frac{\partial v_j}{\partial x_i} - \frac{2}{3}\delta_{ij}\frac{\partial v_k}{\partial x_k}\right), \qquad q_i = \bar{\kappa}\frac{\partial T}{\partial x_i}, \qquad p = \rho R T. \tag{3}$$

Here, ρ represents the density, v_i is the i-th component of the velocity, E is the total specific energy H is the total specific enthalpy. The pressure (p), the density and the temperature (T) obey the ideal gas law. The coefficients $\bar{\mu}$ and $\bar{\kappa}$ are the effective dynamic viscosity and heat conductivity respectively. This coefficients account for both the molecular and turbulent effects (if any):

$$\bar{\mu} = \mu + \mu_t, \qquad \bar{k} = C_p\left(\frac{\mu}{Pr} + \frac{\mu_t}{Pr_t}\right). \tag{4}$$

Notice Stokes's hypothesis and the absence of volume forces have been used to simplify the formulation. For the turbulent cases presented in this paper, the Spalart-Allmaras[23] model will be used, modified to enhance convergence when high order discretizations are used.[11]

The boundary conditions for most problems of interest read:

$$\mathbf{u} = \mathbf{u}_\infty, \quad |\mathbf{x}| \to \infty, \qquad \text{at Far-field,} \tag{5}$$

$$(v_1, v_2, v_3) = 0, \quad T = T_w, \qquad \text{at solid wall (prescribed temperature),} \tag{6}$$

$$(v_1, v_2, v_3) = 0, \quad \mathbf{q}\cdot\mathbf{n} = q_w, \qquad \text{at solid wall (prescribed heat flux).} \tag{7}$$

A. Defect Equations

The defect formulation was first proposed by Le Balleur[24] as a rigorous way to decouple the viscous and inviscid effects around boundary layers and wakes. The idea follows from the observation that the Real Viscous Flow $\mathbf{u}$ (RVF) asymptotes to a solution that satisfies the inviscid Euler equations outside boundary layers and wakes, the so called Equivalent Inviscid Flow $\mathbf{u}_\mathrm{i}$ (EIF).

In principle, one can extend the domain of such inviscid solution all the way down to the wall (or wake) despite the fact that the RVF is different there (see Fig. 1). To guarantee the matching at the edge of the boundary layer, the interaction between both solutions has to be considered. For this, first the differential

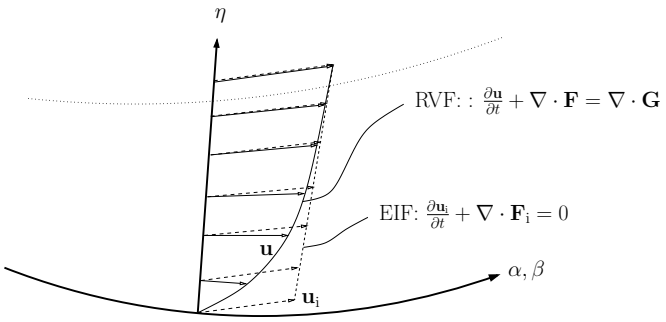

Figure 1: Velocity profiles for the EIF and RVF.

operators that define the RVF and the EIF are subtracted to yield the defect form of the equations:

$$\frac{\partial(\mathbf{u} - \mathbf{u}_\mathrm{i})}{\partial t} + \nabla\cdot(\mathbf{F} - \mathbf{F}_\mathrm{i}) = \nabla\cdot\mathbf{G}. \tag{8}$$

Downloaded by MIT LIBRARIES on August 16, 2022 | http://arc.aiaa.org | DOI: 10.2514/6.2013-857

Then, we define a coordinate transformation from a locally cartesian parameter space (α, β, η) to the physical space (x, y, z) such that (α, β) represents a parametrization of the surface of the body or wake (this mapping is described in the next section in more detail). Now, integrating the defect form over a differential volume like the one described in Figure 2 and taking the limit as $d\alpha$ and $d\beta$ tend to zero, we obtain a boundary condition that the EIF has to satisfy at the wall:

$$\mathbf{F}_\mathrm{i} \cdot \mathbf{n}|_{\eta=0} = -\mathbf{G} \cdot \mathbf{n}|_{\eta=0} + \frac{\partial \mathbf{d}}{\partial t} + \frac{\partial \mathbf{D}_\alpha}{\partial \alpha} + \frac{\partial \mathbf{D}_\beta}{\partial \beta}, \tag{9}$$

where the integrated defects read:

$$\mathbf{d} = \int_0^\infty (\mathbf{u} - \mathbf{u}_\mathrm{i}) d\eta, \qquad \mathbf{D}_\alpha = \int_0^\infty ((\mathbf{F} - \mathbf{F}_\mathrm{i} - \mathbf{G}) \cdot \mathbf{n}_\alpha) d\eta, \qquad \mathbf{D}_\beta = \int_0^\infty ((\mathbf{F} - \mathbf{F}_\mathrm{i} - \mathbf{G}) \cdot \mathbf{n}_\beta) d\eta. \tag{10}$$

Here, the metric factors on the integrals have been omitted for simplicity of notation.

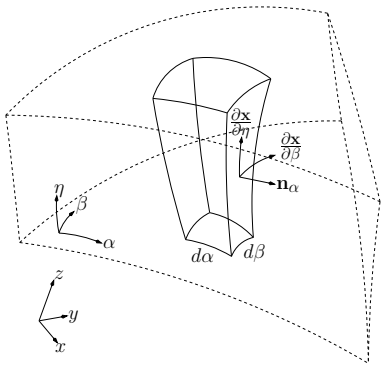

Figure 2: Control volume used to derive the coupling between EIF and RVF. The bottom surface $\eta = 0$ is assumed to be located at a solid wall or over a wake.

The segregated equations are solved on overlapping domains and read:

$$\textbf{EIF:} \quad \frac{\partial \mathbf{u}_\mathrm{i}}{\partial t} + \nabla \cdot \mathbf{F}_\mathrm{i} = 0, \tag{11}$$

$$\mathbf{u}_\mathrm{i} = \mathbf{u}_\infty, \quad |\mathbf{x}| \to \infty, \tag{12}$$

$$\mathbf{F}_\mathrm{i} \cdot \mathbf{n}|_{\eta=0} = -\mathbf{G} \cdot \mathbf{n}|_{\eta=0} + \frac{\partial \mathbf{d}}{\partial t} + \frac{\partial \mathbf{D}_\alpha}{\partial \alpha} + \frac{\partial \mathbf{D}_\beta}{\partial \beta}, \tag{13}$$

$$\textbf{RVF:} \quad \frac{\partial (\mathbf{u} - \mathbf{u}_\mathrm{i})}{\partial t} + \nabla \cdot (\mathbf{F} - \mathbf{F}_\mathrm{i}) = \nabla \cdot \mathbf{G}, \tag{14}$$

$$\mathbf{u} = \mathbf{u}_\mathrm{i}, \quad \text{at } \eta = \infty, \tag{15}$$

$$(v_1, v_2, v_3) = 0, \quad T = T_w \,(\text{or } \mathbf{q} \cdot \mathbf{n} = q_w), \quad \text{at } \eta = 0. \tag{16}$$

From this it is easy to see that the effect of the RVF on the EIF happens at the wall through the integrated defects just discussed. Meanwhile the effect of the EIF on the RVF appears in the governing equations as well as on the boundary conditions at the edge of the boundary layer. Considering that the difference $\mathbf{u} - \mathbf{u}_\mathrm{i}$ is negligible a finite distance away from the wall, then the RVF as well as the defect integrals in the EIF can be truncated at a value $\eta = \eta_\mathrm{ext}$. All in all, the RVF and the EIF can be solved on overlapping meshes where viscous effects are only considered on the RVF close to the wall, as described in Figure 3.

The defect formulation described here is somewhat more complete than the one originally proposed by Le Balleur[21,24] where he used the Thin Shear Layer Navier-Stokes approximation for the viscous fluxes to formally retain curvature correction terms in the integral boundary layer equations. An important advantage of using the full Navier-Stokes is that the defect form is also valid in the vicinity of stagnation points and hence there is no need to initialize the boundary layer there.

B. Coupling boundary conditions and the unicity of the EIF

As it stands, the system described by Eqs. 11-16 does not have a unique solution. As discussed by Murman and Bussing,[25] there is actually infinitely many, since the thermodynamic state of the fluid entering the EIF

Downloaded by MIT LIBRARIES on August 16, 2022 | http://arc.aiaa.org | DOI: 10.2514/6.2013-857

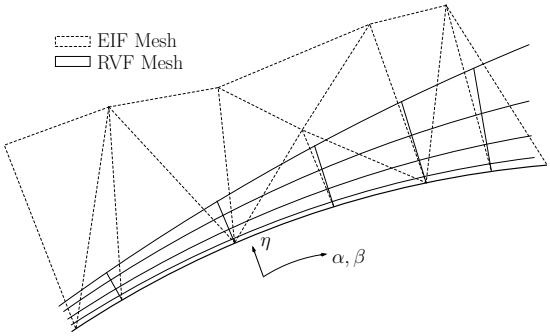

Figure 3: Example of the RVF and EIF meshes used in the defect formulation.

Downloaded by MIT LIBRARIES on August 16, 2022 | http://arc.aiaa.org | DOI: 10.2514/6.2013-857

through the wall is irrelevant as long as the mass flow is correct. Due to this, several boundary conditions are feasible, each of them with their own advantages and disadvantages (see the original paper[25] for a discussion of them). In general, since we are interested in solving the EIF on a coarse mesh (in terms of the boundary layer thickness), we need to choose the boundary conditions so that no entropy layers are generated, as these would require a refinement of the EIF mesh and would ultimately defeat the whole purpose of the viscous/inviscid segregation.

For this reason, we will use the boundary conditions proposed by Whitfield, valid for the case of weakly interacting, iso-energetic flows. These consist of the extrapolation of the pressure and the following conditions on the mass flux and the gradient of the solution:

$$\rho\mathbf{v}\cdot\mathbf{n} = \frac{\partial}{\partial t}\int_0^{\eta_{\text{ext}}} (\rho-\rho_{\text{i}})\, d\eta + \frac{\partial}{\partial \alpha}\int_0^{\eta_{\text{ext}}} (\rho\mathbf{v}-\rho\mathbf{v}_{\text{i}})\cdot\mathbf{n}_\alpha d\eta + \frac{\partial}{\partial \beta}\int_0^{\eta_{\text{ext}}} (\rho\mathbf{v}-\rho\mathbf{v}_{\text{i}})\cdot\mathbf{n}_\alpha d\eta, \tag{17}$$

$$\frac{\partial(\mathbf{v}\cdot\mathbf{n}_\alpha)}{\partial\eta} = 0, \quad \frac{\partial(\mathbf{v}\cdot\mathbf{n}_\beta)}{\partial\eta} = 0, \quad \frac{\partial H}{\partial\eta} = 0, \tag{18}$$

and are meant to substitute Eq. 13.

C. Real Viscous Flow Geometry

As mentioned in the motivation, for this decoupling approach to have any chance of success, the viscous grid needs to follow the boundary layer in such a way that the high order discretization is within the asymptotic convergence regime always. To do so, the RVF domain (again, truncated at a certain $\eta = \eta_{\text{ext}}$) needs to evolve with the solution accordingly. A simple way to do this is to extrude the domain from the wall (or wake) outwards following a predefined direction $\hat{\mathbf{n}}$ that does not necessarily need to coincide with the normal to the surface. The length of the extrusion is dictated by a parameter δ, over the surface of interest, that represents the normal scaling for the boundary layer at a given point on the surface. Based on this, a mapping $G : (\alpha, \beta, \eta) \mapsto (x, y, z)$ is defined by:

$$\mathbf{x} = G_{\text{surf}}(\alpha,\beta) + \delta(\alpha,\beta)\times\eta\times\hat{\mathbf{n}}(\alpha,\beta), \tag{19}$$

where G_{surf} is the parametric representation of the wall (or wake).

Of the two parameters that define the extrusion, $\hat{\mathbf{n}}$ can be generated a priori based on the geometric characteristics of the surface. This only leaves δ to be computed simultaneously with the flow. For this, δ will be evolved on the surface according to the following diffusion-reaction equation:

$$\frac{\partial\delta}{\partial t} = \frac{\delta_{\text{spec}}(\mathbf{u},\delta)-\delta}{\tau} + \Delta_\Gamma(\epsilon\delta), \tag{20}$$

where Δ_Γ is the Laplace-Beltrami operator[26] and the parameters τ and ϵ are constants that dictate the degree of spreading of sharp changes in the indicator. The function $\delta_{\text{spec}}(\mathbf{u},\delta)$ is a measure of the thickness of the boundary layer based on the kinematic displacement thickness and momentum thickness:[27]

$$\delta_{\text{spec}}(\mathbf{u},\delta) \propto \left(\delta_k + \theta_k\left(3.15 + \frac{1.72}{H_k - 1}\right)\right). \tag{21}$$

The boundary conditions for this equation are only required at the edges of the surface. In most of the cases this coincides with the flow leaving the domain, hence of little effect on the solution. The results obtained here have all been obtained with homogeneous Neumann conditions.

D. Arbitrary Lagrangean Eulerian Formulation

The last step in the formulation of the problem consists on taking into account the effect of the evolution of the geometry in the system of PDEs that defines the RVF. For this, an Arbitrary Lagrangean Eulerian (ALE) approach[28] will be used. The main ingredient of the ALE is a mapping $G : (\alpha, \beta, \eta) \mapsto (x, y, z)$ between the reference domain and the physical domain. The goal is the transformation of the general conservation law:

$$\frac{\partial \mathbf{u}}{\partial t} + \nabla \cdot \mathbf{A}(\mathbf{u}, \nabla \mathbf{u}) = \mathbf{f}, \tag{22}$$

into the reference domain. For this, the following derivatives of the mapping are required:

$$\mathbf{v}_G = \frac{\partial G}{\partial t}, \qquad \mathbf{G} = \nabla_{\vec{\alpha}} G, \qquad g = \det(G). \tag{23}$$

The transformed equations in differential form[29] read:

$$\frac{\partial (g\mathbf{u})}{\partial t} + \nabla_{\vec{\alpha}} \cdot \left[g\mathbf{G}^{-1}\mathbf{A}(\mathbf{u}, \mathbf{G}^{-1}\nabla_{\vec{\alpha}}(\mathbf{u})) - g\mathbf{G}^{-1}\mathbf{u} \otimes \mathbf{v}_G \right] = g\mathbf{f}, \tag{24}$$

and can be discretized using a variety of algorithms. In the unsteady case, it can be proved that the ALE does not satisfy the simple case of a uniform flow unless the so-called Geometric Conservation Law is satisfied. Several ways to enforce this are described in the literature.[29] In the cases analyzed here, only steady state solutions are considered, so the Geometric Conservation Law during the time relaxation is not enforced for the sake of simplicity. This has not affected the convergence of the tests shown below.

III. Discretization

All the equations described before are discretized using Finite Element techniques. In particular, the EIF (Eq.11-12,17-18) on the whole domain is discretized using a Hybridized Discontinuous Galerkin scheme (HDG).[30,31] The discrete approximation to the EIF, denoted by $\mathbf{u}_{hi}$, consists of piecewise polynomials of order p, discontinuous across faces of the mesh. Details on the implementation of HDG for the Euler and Navier-Stokes equations, including a discussion on the far field boundary conditions can be found in the literature.[32]

Similarly, the RVF (Eq.14-16) in ALE form is also discretized using an HDG scheme. In this case, the approximation space for the RVF, denoted by $\mathbf{u}_h$, consists on polynomials of order p formed from tensor products of polynomials on the surface and 1D polynomials in the normal direction. As in the case of the EIF, this polynomials are discontinuous across faces of the virtual mesh.

The RVF system requires the value of the EIF or an approximation to it inside the viscous mesh. One possible approach would be to interpolate exactly the value from the EIF, however, this is expensive (since the mesh is evolving) and prone to unstable numerical effects. Some authors have considered the use of the EIF and its gradient at the edge of the viscous mesh[20] to avoid the interpolation in the whole domain, but, this is as hard as the previous option. Here, the value of the EIF at the surface of the viscous mesh will be used. This is:

$$\mathbf{u}_{\mathrm{i}}(\alpha, \beta, \eta) \approx \mathbf{u}_{\mathrm{i}}(\alpha, \beta, 0). \tag{25}$$

Higher order corrections based on the normal gradient at the wall to account for curvature could be easily implemented if required.

Finally, the normal scaling equation is discretized on the surface using a Continuous Galerkin Surface Finite Element Method (SFEM).[26] The approximation space for the discrete normal scaling δ_h consists of continuous piecewise linear polynomials on the surface that defines the wall or wake.

The discrete RVF geometry representation is defined by a high order iso-parametric representation of the surface (inherited from the EIF) combined with a linear normal extrusion as follows:

$$\mathbf{x}(\alpha, \beta, \eta) = \sum_{i=1}^{N} \mathbf{x}_i \phi_i(\alpha, \beta) + \sum_{j=1}^{N_{\mathrm{vertex}}} \delta_{hj} \hat{\mathbf{n}}_j \phi_j^1(\alpha, \beta)\eta, \qquad \eta \in [0, \eta_{\mathrm{ext}}]. \tag{26}$$

Downloaded by MIT LIBRARIES on August 16, 2022 | http://arc.aiaa.org | DOI: 10.2514/6.2013-857

Here, $\mathbf{x}_i$ represents the coefficients of the iso-parametric surface mapping, $\phi_i(\alpha, \beta)$ represents a high order basis function for the surface, $\phi^1_j(\alpha, \beta)$ represents the linear basis functions for δ_{hj} and $\hat{\mathbf{n}}_j$ is the extrusion direction at the edges of the surface triangulation.

The value of the displacement thickness δ_k that appears in the definition of δ_{spec} (Eq. 21) is approximated as a constant inside each surface element $\mathcal{S}_i$, defined as:

$$\delta_k = \frac{\int_{\mathcal{S}_i} \left(\int_0^{\eta_{\text{ext}}} \left(1 - \frac{\mathbf{v}\cdot\mathbf{v}_\text{i}}{\mathbf{v}_\text{i}\cdot\mathbf{v}_\text{i}} \right) d\eta \right) d\mathcal{S}_i}{\int_{\mathcal{S}_i} d\mathcal{S}_i}, \tag{27}$$

which is close to an average over the surface of the element. A similar approach is taken for θ_k:

$$\theta_k = \frac{\int_{\mathcal{S}_i} \left(\int_0^{\eta_{\text{ext}}} \left(1 - \frac{\mathbf{v}\cdot\mathbf{v}_\text{i}}{\mathbf{v}_\text{i}\cdot\mathbf{v}_\text{i}} \right) d\eta \right) \left(\frac{\mathbf{v}\cdot\mathbf{v}_\text{i}}{\mathbf{v}_\text{i}\cdot\mathbf{v}_\text{i}} \right) d\mathcal{S}_i}{\int_{\mathcal{S}_i} d\mathcal{S}_i}. \tag{28}$$

For the time evolution, a method of lines is used in which the time-dependent terms are approximated using an implicit backwards Euler scheme. The nonlinear system defined by the three discrete residuals (EIF, RVF and normal scaling) is solved at each time-step using a Newton-Raphson iteration. For this, the derivatives of all the equations in the system with respect to $\mathbf{u}_h$, $\mathbf{u}_{hi}$ and δ_h are computed analytically. To solve the linear system at each iteration, a sparse direct solver is used.

To converge to a solution, a time relaxation was used in which the time step was multiplied by a fixed constant (2 for laminar flows and 1.5 for turbulent cases) whenever the Newton-Raphson procedure converged in the same number of iteration or less than the previous solution. Otherwise, the time step was reduced by the same factor for the next step. The time relaxation was carried out until a certain time was reached (usually 2 to 3 times L/u_∞). After this, the time-dependent terms were dropped and a steady state solution was computed usually in a few iterations of the Newton-Raphson procedure.

We found that the convergence of SA is ameliorated if a model continuation strategy is followed in which the source terms of the SA model are multiplied by a very small constant ($\alpha_{\text{SA}} = 10^{-3}$) in the beginning and increased by a factor of 5 (up to a value of $\alpha_{\text{SA}} = 1$) after each successful time step. The rationale for this is to reduce the stiffness of the problem in the initial phase when the solution does not satisfy the boundary conditions at the wall and large gradients are present.

IV. Results

The proposed solver will be tested on a series of standard laminar and turbulent cases. Due to limitations on the current implementation of the solver only symmetric (no lift) cases will be considered, yet, this should be enough to highlight the advantages of this approach and indicate areas where there is still room for improvement.

A. Laminar Flat Plate

We first present the solution of the flow over a finite lenght flat plate at Reynolds number $Re = 1 \cdot 10^5$ (based on the chord of the plate) and Mach number $M = 0.3$. For this, a mesh of 15 elements in the normal direction and 30 elements on the flat plate and the wake was used. Three different polynomials orders were considered: $p = 2$, $p = 4$ and $p = 6$. We included a wake in the calculations so that we can try a simple geometry with both a leading and trailing edge. The initial mesh had a uniform thickness of $\delta/L = 5 \cdot 10^{-3}$, roughly 10 times smaller than the final one.

The time relaxation procedure described in the previous section yields a solution like the one shown in Figure 4 for the horizontal velocity profiles over the plate and on the wake. Notice the solution is not sensitive to increasing the polynomial order. This suggests the mesh indicator (see Figure 5) is making a good job at tracking the boundary layer so that the solution is virtually grid converged. At first sight, the velocity profiles in Fig.4 match the Blasius solution for the flat plate without a pressure gradient. To confirm this, Fig. 6a shows the friction coefficient C_f along the plate compared to the well know result by Blasius.[33] Notice the solution virtually overlaps over the entire domain for all the approximation orders used except close to the trailing edge, where it is affected by a a slight pressure gradient due to the wake recovery. Also notice how the C_f presents a jump at the trailing edge that is due to a combination of a sudden change on

Downloaded by MIT LIBRARIES on August 16, 2022 | http://arc.aiaa.org | DOI: 10.2514/6.2013-857

the boundary conditions (from wall to wake) and lack of streamwise resolution. This effect is less pronounced in the mass transpiration applied to the EIF as shown in Fig. 6b.

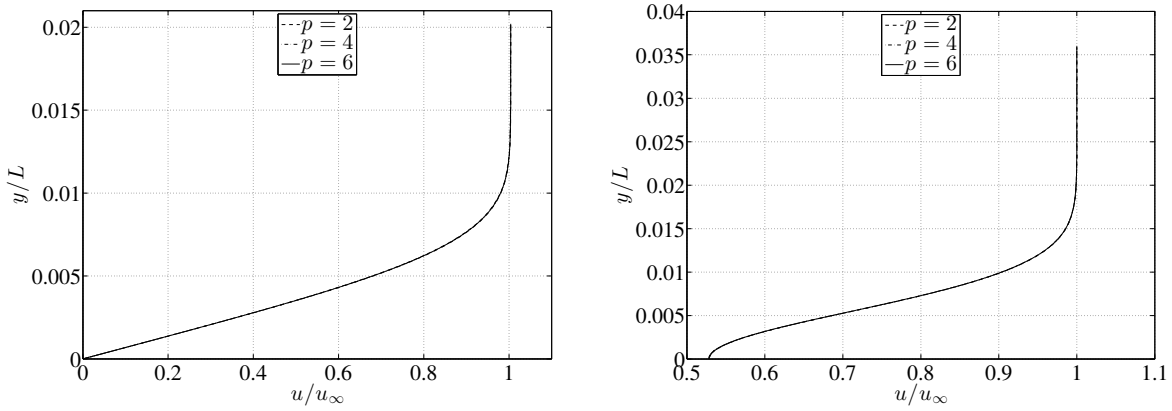

(a) Horizontal velocity profile at $x/L = 0.5$.

(b) Horizontal velocity profile at $x/L = 1.5$ (on the wake).

Figure 4: Horizontal velocity profiles for the flow around a finite length flat plate. For this case $Re = 1 \cdot 10^5$ and $M_\infty = 0.3$. The results were computed using polynomials of order $p = 2$, $p = 4$ and $p = 6$.

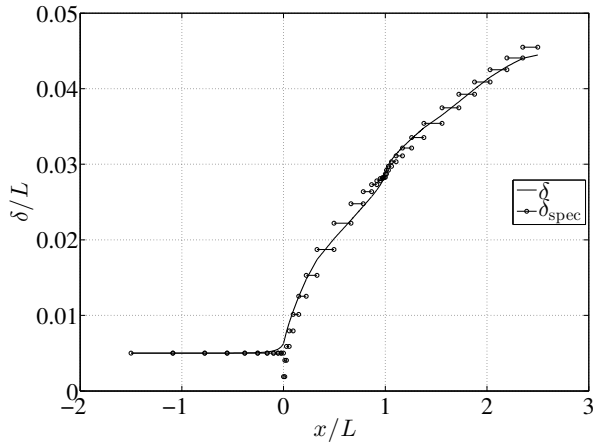

Figure 5: Normal scaling δ and thickness indicator δ_{spec} for the case of the laminar flow over a finite flat plate at $Re = 1 \cdot 10^5$ and $M_\infty = 0.3$. In this case the flow was computed using polynomials of order $p = 6$.

Downloaded by MIT LIBRARIES on August 16, 2022 | http://arc.aiaa.org | DOI: 10.2514/6.2013-857

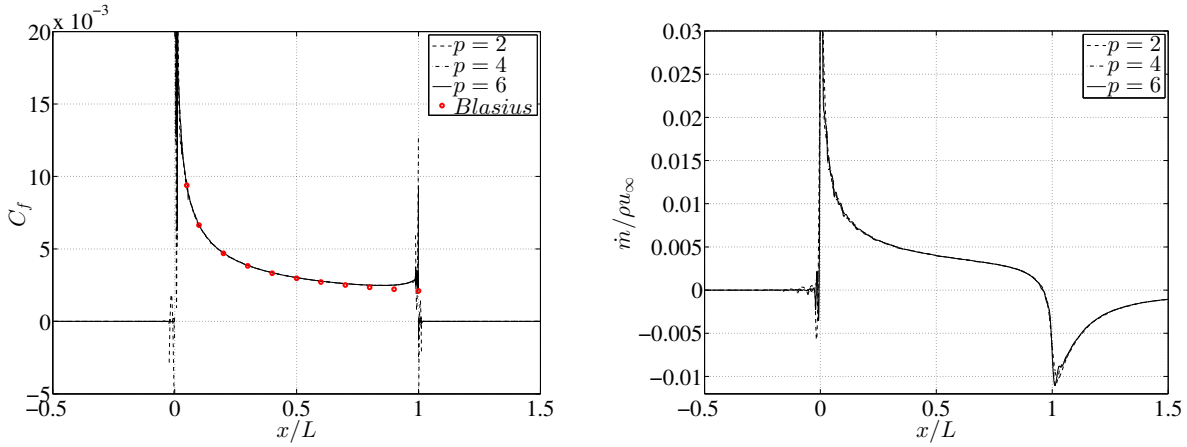

(a) Friction coefficient

(b) Mass transpiration

Figure 6: Friction coefficient (left) and mass transpiration (right) over the surface of the finite flat plate at $Re = 1 \cdot 10^5$ and $M_\infty = 0.3$ using different polynomial orders.

B. Laminar flow over a bump

The next case we would like to present is the laminar flow over a small sinusoidal bump at a Reynolds number of $Re = 1 \cdot 10^5$ (based on a characteristic computational length L) and Mach number $M = 0.2$. The bump extends one characteristic length along a flat plate and has a height of $h/L = 10^{-2}$. The viscous mesh for this case consists on 30 elements on the surface of the geometry and 12 elements in the normal direction. Three different polynomials orders were considered for the solution: $p = 2$, $p = 4$ and $p = 6$. The initial mesh used for the computation was uniformly set to $\delta/L = 10^{-3}$, 20-40 times smaller than the final mesh, that is represented in Fig. 7.

The interest in this case lies on the fact that this combination of bump height and Reynolds number produces a laminar separation bubble downwind of the bump that eventually reattaches. One can distinguish such separation bubble in Fig.8 where the horizontal component of the velocity is plotted. One can also identify the separation bubble by looking at the friction coefficient over the bump (Fig. 9a) or by a direct plot of the velocity profiles there (Fig. 9b). Notice how the solution is still changing as the polynomial order is increased, which suggests a possible lack of resolution in our mesh, most likely in the streamwise direction. Further numerical tests are required to asses this issue. In any case, the approach based on adapting on the fly has proven robust and provides meshes that follow the viscous features as desired (see Fig. 10). These features (thinning, separation, reattachment, etc.) are properly transferred to the inviscid solver through the coupling at the wall as shown in Fig. 11.

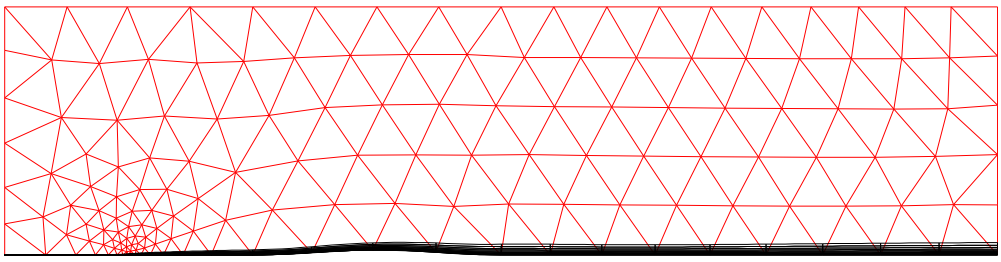

Figure 7: Viscous (black) and Inviscid (red) meshes obtained during the computation of the laminar flow over a bump.

Downloaded by MIT LIBRARIES on August 16, 2022 | http://arc.aiaa.org | DOI: 10.2514/6.2013-857

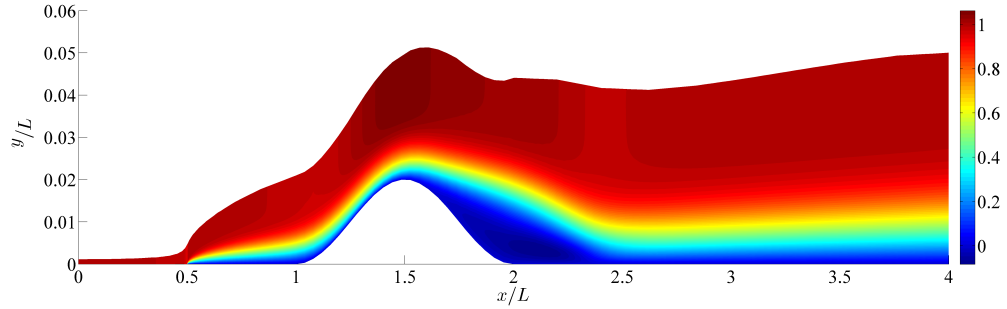

Figure 8: Horizontal component of the velocity field u/u_∞ over a bump computed using polynomials of order $p = 6$. For visualization purposes, axis are NOT to scale.

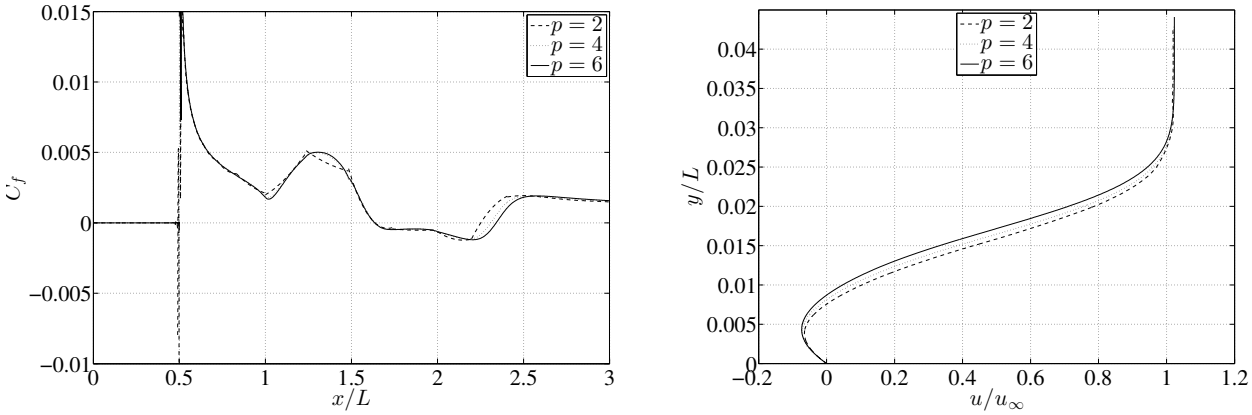

(a) Friction coefficient

(b) Horizontal Velocity profile at station $x/L = 2$

Figure 9: Friction coefficient (left) and horizontal velocity profile (right) across the separation bubble computed using different polynomial orders.

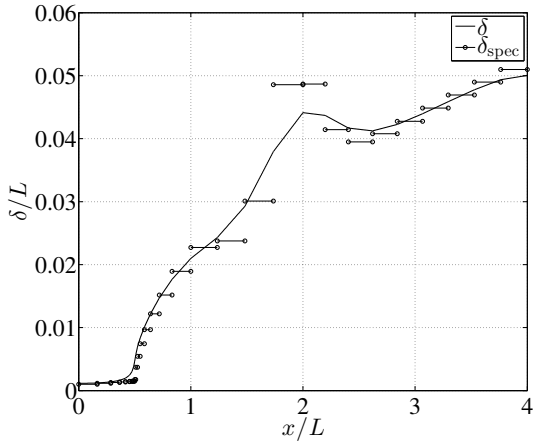

Figure 10: Normal scaling δ and thickness indicator δ_{spec} for the case of the laminar flow over a bump as computed using polynomials of order $p = 6$. Notice the peak in the indicator over the extent of the separation bubble.

Downloaded by MIT LIBRARIES on August 16, 2022 | http://arc.aiaa.org | DOI: 10.2514/6.2013-857

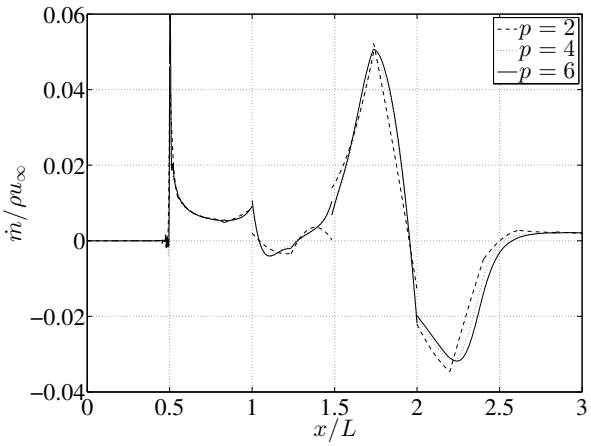

Figure 11: Mass transpiration fluxes obtained in the case of a laminar bump for different polynomial orders.

Downloaded by MIT LIBRARIES on August 16, 2022 | http://arc.aiaa.org | DOI: 10.2514/6.2013-857

C. Laminar flow over a NACA 0006 airfoil

In the previous examples, we tested the solver in geometries that despite being simple were able to produce effects such as wakes or moderate separation. In this same spirit, we now move on to the case of symmetric laminar airfoil. The goal here is to test how it behaves in the presence of a stagnation point as well as very mild separation at the trailing edge. In particular, we will solve the flow over half a NACA 0006 airfoil, modified to have a closed trailing edge. For this, the following equation is used to describe the top surface of the airfoil:

$$y_t = \frac{t}{0.2}c\left[0.2969\sqrt{\frac{x}{c}} - 0.1260\left(\frac{x}{c}\right) - 0.3516\left(\frac{x}{c}\right)^2 + 0.2843\left(\frac{x}{c}\right)^3 - 0.1036\left(\frac{x}{c}\right)^4\right], \tag{29}$$

where the last term is different with respect to the standard NACA 4-digit series. For this case we will set the Reynolds number to $Re = 1 \cdot 10^5$ (based on the chord of the airfoil c) and the Mach number to $M = 0.3$. The viscous mesh in this case consists of 44 elements in the surface direction and 12 elements in the normal. Solutions up to polynomial order $p = 4$ were computed on this mesh. The initial condition for the normal scaling was set to $\delta = 5 \cdot 10^{-3}$. The meshes obtained in the final iteration are plotted in Fig. 12.

To asses how well the scheme behaves around stagnation points, we can have a look at the Mach number and density profiles around it. These are shown in Fig. 13. One of the main advantages of our approach is the fact that it does not depend on any thin shear layer approximations, hence, it does not require an initialization of the boundary layer at the stagnation point nor identifying it a priori. The only conditions we set in this example are the symmetry boundary conditions on the line $y = 0$.

To confirm that the solution is correct, we can have a look at surface quantities. In particular, we can compare our solution against the widely adopted solver Xfoil[34] for the same parameters of the problem. The results in Fig. 14 show the good agreement in friction coefficient and transpiration velocity around the leading edge for different approximation orders. There, we can also see a very mild separation happening at the trailing edge that is picked up by the normal scaling indicator (see Fig. 15) and modifies the pressure field around the trailing edge (see Fig. 16) accordingly. The discrepancies with Xfoil at the trailing edge might be due to the fact that we propagate a laminar wake while Xfoil prescribes transition there.

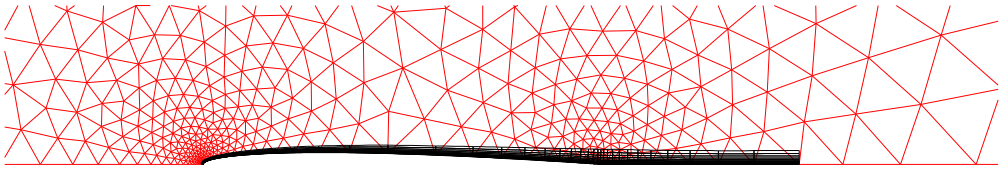

Figure 12: Viscous (black) and Inviscid (red) meshes obtained from the computation of the laminar flow over a NACA 0006 airfoil.

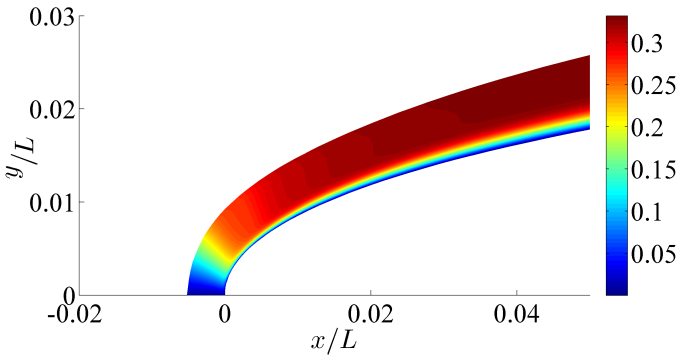

(a) Mach number M

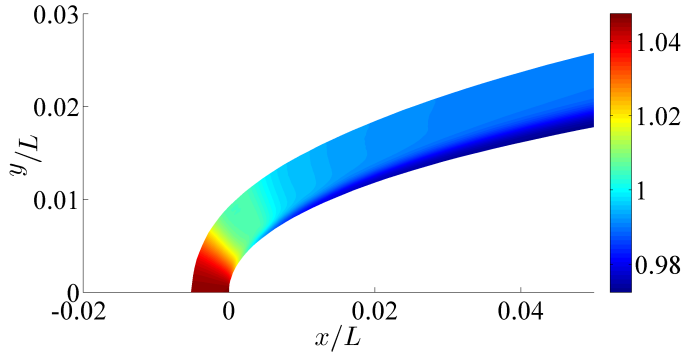

(b) Density ρ

Figure 13: Mach number (left) and density (right) fields in the vicinity of the leading edge of the NACA 0006 airfoil computed using polynomials of order $p = 4$.

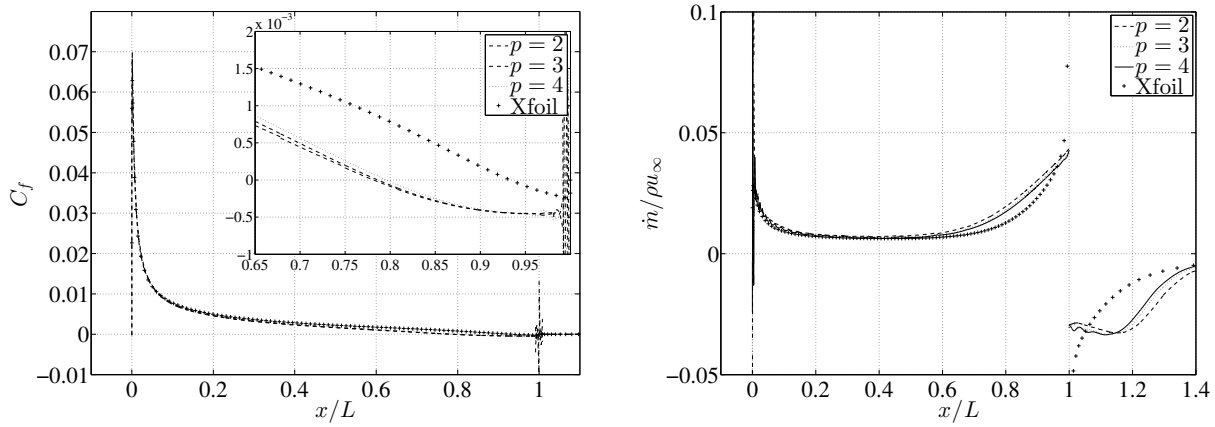

(a) Friction coefficient

(b) Mass Transpiration flux

Figure 14: Friction coefficient (left) and mass transpiration flux (right) for the case of the NACA 0006 airfoil.

D. Turbulent flow over a flat plate

Now we turn our attention to the case of turbulent flows. For this, we will solve the RANS equations using a modified version of the Spalart-Allmaras model suitable for a high order discretization.[11] It is a well known fact that the solution of the RANS equations is significantly harder that the solution of laminar flows due to severe restrictions in mesh size as well as the strong nonlinearity of most closure models. For this reason, we will start from the very simple case of a finite length flat plate. Namely, we are interested in the fully

Downloaded by MIT LIBRARIES on August 16, 2022 | http://arc.aiaa.org | DOI: 10.2514/6.2013-857

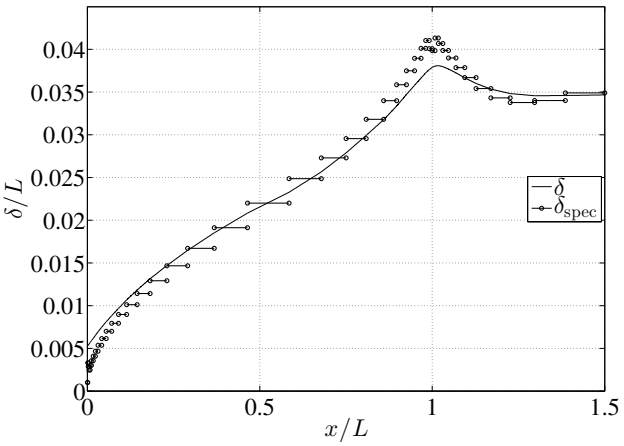

Figure 15: Normal scaling δ and thickness indicator δ_{spec} for the case of the laminar flow over a NACA 0006 computed using polynomials of order $p = 4$. Notice the peak in the indicator due to mild separation at the trailing edge.

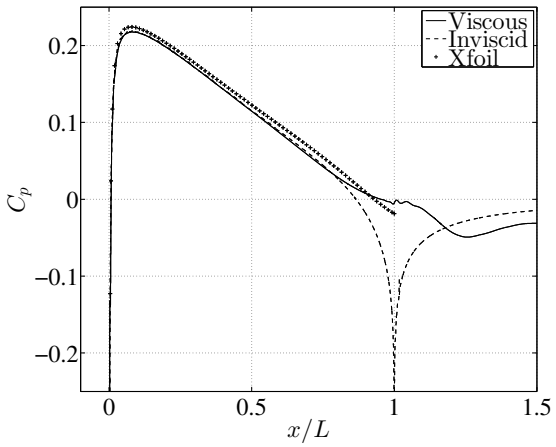

Figure 16: Pressure coefficient for the case of the NACA 0006 airfoil computed using polynomials of order $p = 4$. As comparison, the results obtained without boundary layer and using Xfoil are also included.

Downloaded by MIT LIBRARIES on August 16, 2022 | http://arc.aiaa.org | DOI: 10.2514/6.2013-857

turbulent flow over a finite flat plate at Reynolds number $Re = 10^7$ (based on the length of the plate L) and Mach number to $M = 0.5$. The mesh used for the viscous solution consists on 36 elements over the plate and the wake and 10 elements in the normal direction of polynomial order up to $p = 4$.

We set the initial mesh thickness to $\delta/L = 5 \cdot 10^{-5}$ and using time relaxation, combined with model continuation, we reach steady state. The two most relevant fields in the solution are the horizontal velocity and the SA working variable, that are plotted in Fig. 17. There we can see how the normal scaling mimics the growth of the boundary layer and the wake adequately. If we look at their profiles at a point in the middle of the plate ($Re_x = 5 \cdot 10^6$), contained in Fig.18, we can see how the velocity (once properly scaled) closely follows the law of the wall. Also, the SA working variable shows the expected shape.

Some surface quantities of interest are plotted in Figs. 19 and 20. In particular, Fig. 19b shows the friction coefficient computed using different orders of approximation and compared to the analytical solution proposed by Prandtl.[33] The results are in good agreement although they do not match perfectly. This might be due to the limited resolution in the normal direction, dictated by a combination of the normal scaling δ (see Fig. 20a), the distribution of nodes in the reference coordinate η and the number of such nodes (or elements). Ideally, one would seek a mesh distribution such that $y_1^+ = \mathcal{O}(1)$ for the first node off the wall. In Fig. 20b we plot the value y_1^+. As we can see, the criterion is only satisfied very close to the leading edge. More refined meshes ought to be used to find the source of such discrepancy.

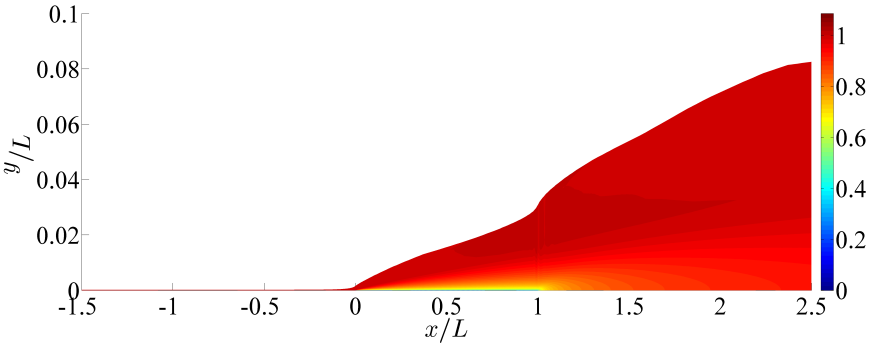

(a) Horizontal velocity u/u_∞

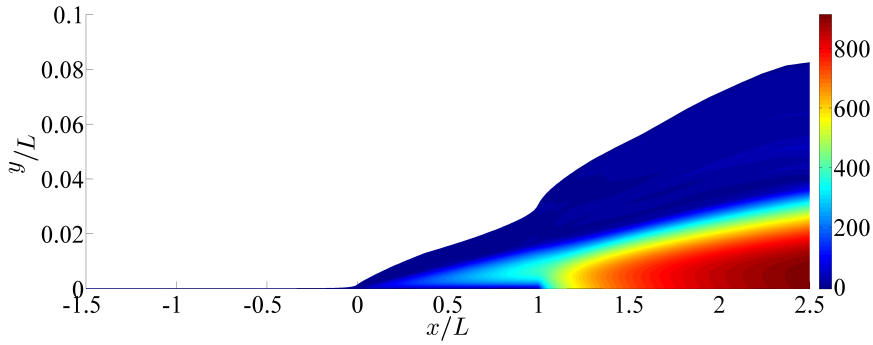

(b) SA working variable ν/ν_∞

Figure 17: Horizontal velocity field (top) and SA variable field (bottom) for the case of the turbulent flat plate. For visualization purposes, axis are NOT to scale.

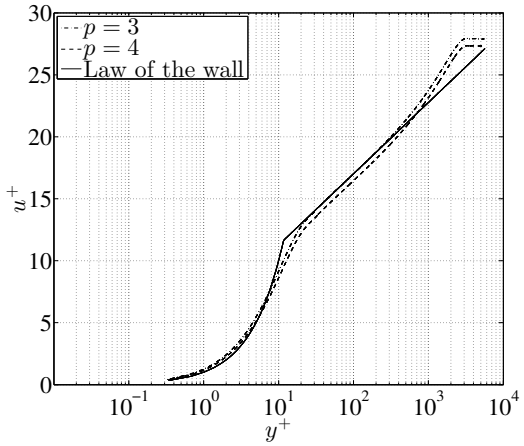

(a) Normalized velocity profile u^+ vs. y^+

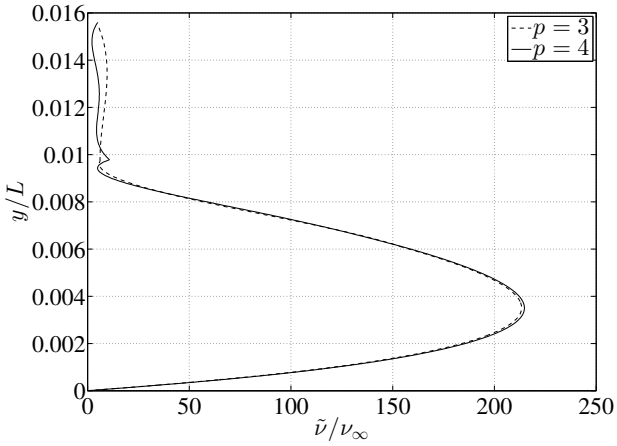

(b) SA working variable ν/ν_∞

Figure 18: Profiles of the solution at $Re_x = 5 \cdot 10^6$ for the turbulent flat plate.

E. Turbulent flow over a NACA 0008 airfoil

Last, we would like to show some results for the turbulent flow around a NACA 0008 airfoil at Reynolds number $Re = 10^7$ (based on the aerodynamic chord) and Mach number $M = 0.3$. As in the case of the laminar airfoil, only half the geometry will be computed. Also, Eq. 29 is used to generate a closed trailing edge. The mesh used for the viscous solution consists of 43 elements along the surface and 15 in the normal direction. In this case, solutions up to $p = 3$ were computed.

Downloaded by MIT LIBRARIES on August 16, 2022 | http://arc.aiaa.org | DOI: 10.2514/6.2013-857

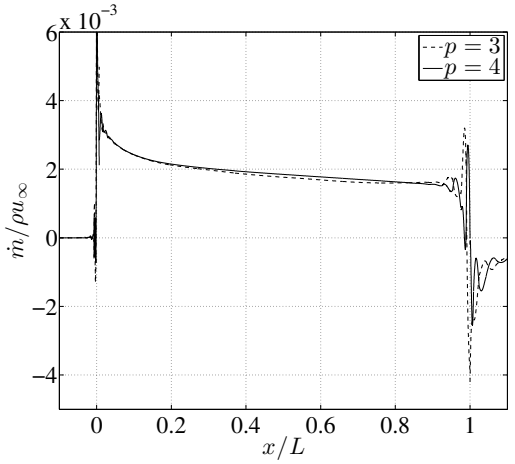

(a) Mass transpiration

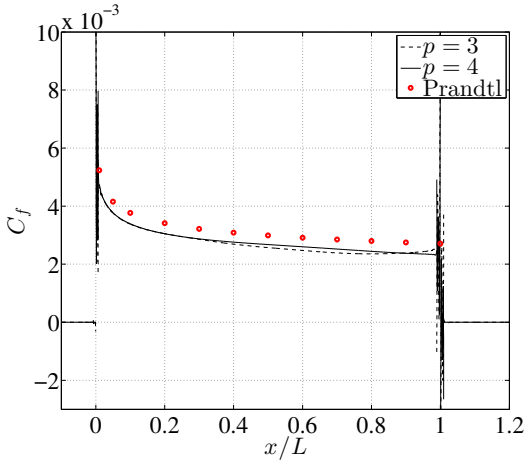

(b) Friction coefficient

Figure 19: Mass transpiration (left) and friction coefficient (right) over the turbulent flat plate for different approximation orders.

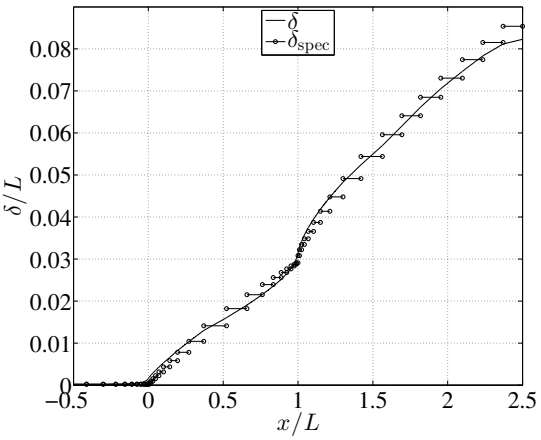

(a) Normal scaling δ and thickness indicator δ_{spec}

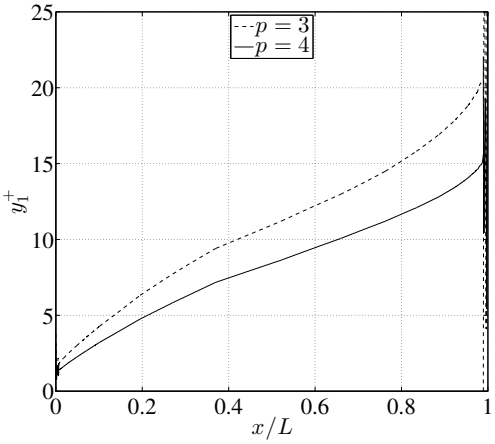

(b) Distance of first node of the wall y_1^+

Figure 20: Normal scaling and thickness indicator (left) and y^+ for the first node off the wall (right) in the case of the turbulent flat plate.

After the usual time relaxation, a steady state was found for the viscous mesh (Fig. 21) as well as the solution (Fig. 22). In this case, the ratio of maximum to minimum normal scaling δ is of order 200 ($6{\cdot}10^{-2}/3{\cdot}10^{-4}$) and is generated automatically without user intervention. We believe this is one of the main advantages of the proposed approach. As in the case of the laminar airfoil, we compare our solution with the one provided by Xfoil[34] for this same geometry. In particular, Fig. 23 contains the surface quantities of interest for this flow. As we can see there, the friction coefficient agrees with Xfoil provided there is enough resolution close to the wall to properly capture the laminar sublayer (notice the discrepancy for $p = 2$) while the mass transpiration flux agrees well in both cases.

F. A word on the trailing edge conditions

All the result presented above are fully converged solutions where the residual of the final steady state iteration could be driven to values close to machine precision in absolute terms ($\|R\| < 10^{-10}$). In most instances, the computed fields are clean and free from oscillations, yet, some derived quantities like the

Downloaded by MIT LIBRARIES on August 16, 2022 | http://arc.aiaa.org | DOI: 10.2514/6.2013-857

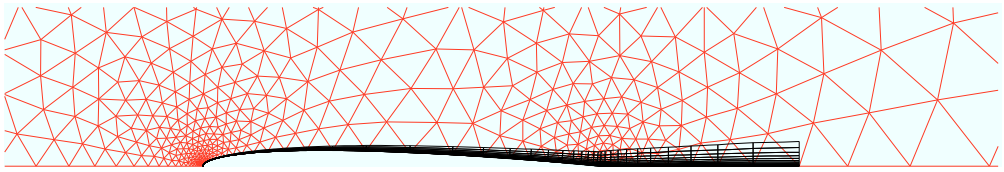

Figure 21: Viscous (black) and Inviscid (red) meshes obtained during the computation of the turbulent flow over a NACA 0008 airfoil.

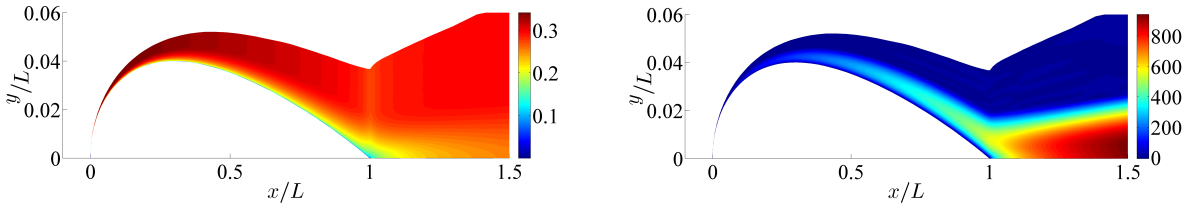

(a) Mach number M

(b) SA variable ν/ν_∞

Figure 22: Mach number (left) and SA variable (right) for the turbulent NACA 0008. Axis are NOT to scale for visualization purposes

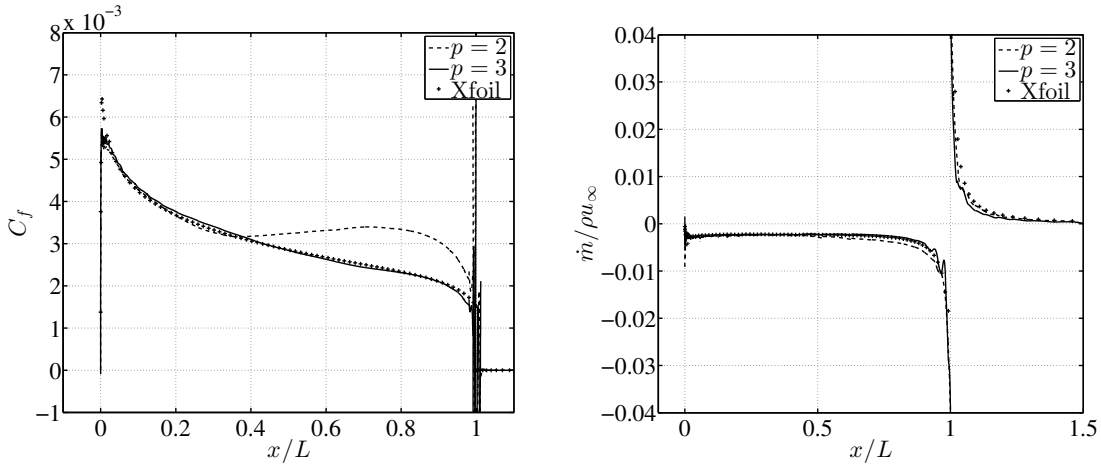

(a) Friction coefficient

(b) Mass Transpiration flux

Figure 23: Friction coefficient (left) and mass transpiration flux (right) for the case of the turbulent flow over a NACA 0008 airfoil.

mass transpiration or the friction coefficient might present them. In some cases these oscillations are due to singularities in the leading edge, such as the case of the flat plate, and appear when we try to approximate them with a high order polynomial. These are usually mild and rarely prevent convergence of the iteration.

On the other hand, we have the oscillations produced at the trailing edge, that in most cases make the friction coefficient a small distance away from it completely useless. One could argue that this is exactly the opposite behavior as the leading edge in that the friction coefficient suddenly changes from a finite value on the wall to zero at the wake, hence the oscillation. Our concern is that we have found this to be a typical failure mode of the iteration in which a high frequency solution at the trailing edge grows until it corrupts the mass transpiration and the iteration stagnates. We are still working on the solution to this problem and evaluating other boundary conditions that might help alleviate this issue.

Downloaded by MIT LIBRARIES on August 16, 2022 | http://arc.aiaa.org | DOI: 10.2514/6.2013-857

V. Conclusions and future work

We have presented a new interactive boundary layer solver and tested it on some simple symmetric cases in 2D. The results indicate that this technique is capable of self adapting the boundary layer grid based on the boundary layer thickness, and using a segregated approach based on the defect formulation, couple it to the inviscid solver at the wall in a monolithic manner.

In the future, the solver will be extended to treat cases with lift as well as coupling it to other inviscid models such as full potential or panel methods. These simplified models might be the key to the extension of this technique to 3D flows due to computational savings, simplicity of wake treatment as well as compatibility of the coupling conditions.

Acknowledgments

N. C. Nguyen and J. Peraire would like to acknowledge the Singapore-MIT Alliance and the Air Force Office of Scientific Research under the grant FA9550-12-0357 for partially supporting this work. M. Drela would like to aknowledge the support of The Boeing Company (technical supervisors David P. Young and Mori Mani). D. Moro would like to acknowledge the support of LaCaixa Foundation and The Boeing Company.

We would like to extend our gratitude to David P. Young, Philippe Spalart and Steven R. Allmaras for their helpful comments and suggestions. Special thanks to Xevi Roca for many fruitful conversations and his help generating some of the high order meshes used in this work.

References

[1]Reed, N. and Hill, T., "Triangle mesh methods for the neutron transport equation," Tech. Rep. LA2 UR-73-479, Los Alamos Scientific Laboratory, 1973.

[2]Cockburn, B. and Shu, C., "The local discontinuous Galerkin method for time-dependent convection-diffusion systems," *SIAM Journal on Numerical Analysis*, Vol. 35, No. 6, 1998, pp. 2440–2463.

[3]Peraire, J. and Persson, P.-O., "The compact Discontinuous Galerkin (CDG) method for elliptic problems," *SIAM Journal on Scientific Computing*, Vol. 30, No. 4, 2008, pp. 1806–1824.

[4]Hartmann, R., Held, J., and Leicht, T., "Adjoint-based error estimation and adaptive mesh refinement for the RANS and $k\omega$ turbulence model equations," *Journal of Computational Physics*, Vol. 230, No. 11, 2011, pp. 4268–4284.

[5]Yano, M., Modisette, J. M., and Darmofal, D., "The importance of mesh adaptation for higher-order discretizations of aerodynamic flows," *20th AIAA Computational Fluid Dynamics Conference*, 2011.

[6]Fidkowski, K. and Darmofal, D., "A triangular cut–cell adaptive method for high–order discretizations of the compressible Navier–Stokes equations," *Journal of Computational Physics*, Vol. 225, 2007, pp. 1653–1672.

[7]Persson, P. and Peraire, J., "Curved mesh generation and mesh refinement using Lagrangian solid mechanics," *47th AIAA Aerospace Sciences Meeting and Exhibit*, 2008.

[8]Barter, G. and Darmofal, D., "Shock capturing with PDE-based artificial viscosity for DGFEM: Part I. Formulation," *Journal of Computational Physics*, Vol. 229, No. 5, 2010, pp. 1810–1827.

[9]Cuong, N. C. and Peraire, J., "An Adaptive Shock-Capturing HDG Method for Compressible Flows," *20th AIAA Computational Fluid Dynamics Conference*, 2011.

[10]Moro, D., Nguyen, N. C., Peraire, J., and Gopalakrishnan, J., "A hybridized Discontinuous Petrov-Galerkin method for compressible flows (AIAA Paper 2011-197)," *49th AIAA Aerospace Sciences Meeting*, Orlando, FL, USA, Jan 2011.

[11]Moro, D., Nguyen, N. C., and Peraire, J., "Navier-Stokes solution using Hybridizable Discontinuous Galerkin methods," *20th AIAA Computational Fluid Dynamics Conference*, 2011.

[12]Bussoletti, J., Johnson, F., Bieterman, M., Hilmes, C., Melvin, R., Young, D., and Drela, M., "TRANAIR- Solution adaptive CFD modeling for complex 3D configurations," *Recent developments and applications in aeronautical CFD*, 1993, p. 10.

[13]Allmaras, S. R., Bussoletti, J. E., Hilmes, C. L., Johnson, F. T., Melvin, R. G., Tinoco, E. N., Venkatakrishnan, V., Wigton, L. B., and Young, D. P., "Algorithm Issues and Challenges Associated with the Development of Robust CFD Codes," *Variational Analysis and Aerospace Engineering*, Springer New York, 2009.

[14]Johnson, F., Tinoco, E., and Yu, N., "Thirty years of development and application of CFD at Boeing Commercial Airplanes, Seattle," *Computers & Fluids*, Vol. 34, No. 10, 2005, pp. 1115–1151.

[15]Drela, M. and Giles, M., "Viscous-inviscid analysis of transonic and low Reynolds number airfoils," *AIAA journal*, Vol. 25, No. 10, 1987, pp. 1347–1355.

[16]Drela, M., "Integral boundary layer formulation for blunt trailing edges," *7 th AIAA Applied Aerodynamics Conference, Seattle, WA*, 1989, pp. 59–68.

[17]Drela, M., "Newton solution of coupled viscous/inviscid multielement airfoil flows," *21st AIAA Fluid Dynamics, Plasma Dynamics and Lasers Conference, Seattle, WA*, 1990.

[18]Mughal, B. and Drela, M., "A calculation method for the three-dimensional boundary-layer equations in integral form," *AIAA Paper 93-0786*, 1993.

Downloaded by MIT LIBRARIES on August 16, 2022 | http://arc.aiaa.org | DOI: 10.2514/6.2013-857

[19]Nishida, B. and Drela, M., *Fully simultaneous coupling of the full potential equation and the integral boundary layer equations in three dimensions*, Ph.D. thesis, Massachusetts Institute of Technology, 1996.

[20]Allmaras, S., *A coupled Euler/Navier-Stokes algorithm for 2-D unsteady transonic shock/boundary-layer interaction*, Ph.D. thesis, Massachusetts Institute of Technology, 1989.

[21]Le Balleur, J., "Calcul par intéraction visqueux-non visqueux des écoulements compressibles fortement décollés aux grandes portances sur profils d'ailes et voilures," Tech. Rep. 92-184, ONERA, TP, 1992.

[22]Le Balleur, J., "Computation of viscous flows over airfoils including separation, with a coupling approach," TM 77079, NASA, 1983.

[23]Spalart, P. and Allmaras, S., "A one-equation turbulence model for aerodynamic flows," *La recherche aérospatiale*, Vol. 1, No. 1, 1994, pp. 5–21.

[24]Le Balleur, J., "Calculation method for transonic separated flows over airfoils including spoiler effects," *Eighth International Conference on Numerical Methods in Fluid Dynamics*, Springer, 1982, pp. 315–322.

[25]Murman, E. and Bussing, T., "Numerical and Physical Aspect of Aerodynamic Flows II," *Numerical and Physical Aspect of Aerodynamic Flows II*, 1984.

[26]Dziuk, G. and Elliott, C., "Surface finite elements for parabolic equations," *Journal of Computational Mathematics*, Vol. 25, No. 4, 2007, pp. 385–407.

[27]Drela, M., *Two-dimensional transonic aerodynamic design and analysis using the Euler equations*, Ph.D. thesis, Massachusetts Institute of Technology, 1986.

[28]Donea, J., Huerta, A., Ponthot, J., and Rodríguez-Ferran, A., "Arbitrary Lagrangian–Eulerian methods," *Encyclopedia of Computational Mechanics*, 2004.

[29]Persson, P., Bonet, J., and Peraire, J., "Discontinuous Galerkin solution of the Navier-Stokes equations on deformable domains," *Computer Methods in Applied Mechanics and Engineering*, Vol. 198, No. 17-20, 2009, pp. 1585–1595.

[30]Nguyen, N. C., Peraire, J., and Cockburn, B., "An implicit high-order hybridizable Discontinuous Galerkin method for linear convection-diffusion equations," *Journal of Computational Physics*, Vol. 228, No. 9, 2009, pp. 3232–3254.

[31]Nguyen, N. C., Peraire, J., and Cockburn, B., "An implicit high-order hybridizable Discontinuous Galerkin method for nonlinear convection-diffusion equations," *Journal of Computational Physics*, Vol. 228, No. 23, 2009, pp. 8841–8855.

[32]Peraire, J., Nguyen, N. C., and Cockburn, B., "A hybridizable Discontinuous Galerkin method for the compressible Euler and Navier-Stokes equations (AIAA Paper 2010-363)," *Proceedings of the 48th AIAA Aerospace Sciences Meeting and Exhibit*, Orlando, FL, USA, Jan 2010.

[33]Schlichting, H. and Gersten, K., *Boundary layer theory*, Springer, 2004.

[34]Drela, M., "XFOIL: An analysis and design system for low Reynolds number airfoils," *Low Reynolds Number Aerodynamics*, edited by T. Mueller, No. 54 in Lecture Notes in Engineering, Springer-Verlag, 1989.

Downloaded by MIT LIBRARIES on August 16, 2022 | http://arc.aiaa.org | DOI: 10.2514/6.2013-857